Simultaneous Inversion of Multiple Faults' Parameters From InSAR Data Using a Genetic Algorithm

Cameron Saylor[1], John B. Rundle[2], and Andrea Donnellan[3]

[1]University of California, Davis
[2]University of California - Davis
[3]Jet Propulsion Laboratory, California Institute of Technology & University of Southern California

November 22, 2022

Abstract

Interferometric synthetic-aperture radar (InSAR) interferograms contain valuable information about the fault systems hidden beneath the surface of the Earth. In a new approach, we aim to fit InSAR ground deformation data using a volumetric distribution of multiple seismic point sources whose parameters are found by a genetic algorithm. The resulting source distribution could provide another useful tool in solving the difficult problem of accurately mapping earthquake faults. To test the algorithm, we first apply it to synthetic data, followed by applications to an ALOS-2 InSAR interferogram. We report first results and discuss advantages and disadvantages of this approach.

Simultaneous Inversion of Multiple Faults' Parameters From InSAR Data Using a Genetic Algorithm

Cameron Saylor[1], John B. Rundle[1,2,3], and Andrea Donnellan[4]

[1]University of California, Davis, Department of Physics and Astronomy
[2]University of California, Davis, Department of Earth and Planetary Science
[3]Sante Fe Institute, Sante Fe, NM
[4]Jet Propulsion Laboratory, California Institute of Technology

Key Points:

- inversion for the parameters of multiple faults at once

Corresponding author: Cameron Saylor, `ccsaylor@ucdavis.edu`

Abstract

Interferometric synthetic-aperture radar (InSAR) interferograms contain valuable information about the fault systems hidden beneath the surface of the Earth. In a new approach, we aim to fit InSAR ground deformation data using a volumetric distribution of multiple seismic point sources whose parameters are found by a genetic algorithm. The resulting source distribution could provide another useful tool in solving the difficult problem of accurately mapping earthquake faults. To test the algorithm, we first apply it to synthetic data, followed by applications to an ALOS-2 InSAR interferogram. We report first results and discuss advantages and disadvantages of this approach.

1 Introduction

Significant errors can occur in fault geometry and slip dislocation models as a result of volumetric distributions of sources not well represented by simple planar or rectangular fault models. For this reason, it is necessary to utilize all of the tools available to improve estimates of fault geometry and location. One such tool is interferometric synthetic aperture radar (InSAR), which provides maps of surface deformation that contain valuable information about the complexity of the fault system giving rise to the image (Bürgmann et al., 2000). InSAR is a radar technique that uses a synthetic aperture radar (SAR) mounted on a satellite to image the same area at two different times, and uses those images to determine the differences in phase of the waves that return to the SAR. Since the wavelength of the electromagnetic waves emitted by the SAR is known, the phase difference between the images can be used to calculate their difference in line-of-sight distance to the satellite. The result is a map of the line-of-sight ground deformation of the imaged area that occurred between the times that the original SAR images were taken (Jet Propulsion Laboratory, California Institute of Technology, 2014).

Previous work has been performed that aimed to invert the ground deformation contained in InSAR interferograms to find the geometry of faults that could cause the observed ground deformation. Such methods rely on having a model that depends on various parameters that can recreate the desired dataset. For seismology, a commonly used model is Okada's analytical solutions for the surface deformation due to faults in an elastic half space, which can model ground deformation due to either point or finite rectangular seismic sources (Okada, 1985).

The inversion detailed in Bagnardi and Hooper (2018), for example, utilizes an Okada rectangular fault model described by 9 parameters: length, width, depth, strike angle, dip angle, X and Y-coordinates, uniform slip in the strike direction and uniform slip in the dip direction (Bagnardi & Hooper, 2018). Their approach uses a Bayesian inversion to determine a posterior probability density function (PDF) which describes how well a set of parameters can explain a given dataset based on their uncertainties and taking into account prior information in the form of a joint prior PDF. A Monte-Carlo Markov Chain utilizing the Metropolis-Hastings algorithm is then used to efficiently search the parameter space by taking steps in the prior PDF to get new sets of parameter values and comparing the likelihood of the new model to the previous step (Hastings, 1970). After an appropriate number of iterations, the sampling done by the algorithm approximates the desired posterior PDFs of each of the parameters, which can be used to estimate their most likely values. Jo et al. (2017) performed a different type of inversion for the $M_W = 6.0$ 2014 South Napa earthquake for a similar set of parameters for a rectangular fault model (Jo et al., 2017). They used two separate inversions in their analysis, the first being a Monte Carlo simulation of 10000 iterations to find the fault parameters. A second least squares inversion was performed to find the slip distribution over the rectangular fault plane.

Aside from Monte Carlo methods, there are other analysis techniques that have been used to invert InSAR interferograms. Feng et al. (2013) utilized a method of inversion called multipeak particle swarm optimization (M-PSO) to study the 2011 $M_W = 6.8$ Burma earthquake (Feng et al., 2013). A PSO works by first defining a population (or swarm) of candidate solutions to a problem and then moving them throughout the parameter space to find the optimal solution. The particles move according to a "velocity" that is based on each particle's own best known position in the parameter space as well as the best known position of the other particles (Kennedy & Eberhart, 1995). Wen et al. (2016) and Li et al. (2020) also used a M-PSO inversion in their analyses of the 2015 $M_W = 6.5$ Pishan earthquake and the 2013 $M_W = 6.6$ Lushan earthquake, respectively, while additionally adding a second inversion for the slip distribution on the fault plane (Wen et al., 2016; Li et al., 2020).

There have also been advances in specific aspects of the inversion, such as the slip distribution. Liu and Xu (2019) developed another method for the joint inversion of coseismic and postseismic fault slip from InSAR data called LogSIM, which uses a logarithmic model solved by a nonlinear least squares curve fitting function (Liu & Xu, 2019). Zhang et al. (2008) solved the slip distribution inverse problem with a model using triangular dislocation elements to more accurately model the 3D fault surface (Zhang et al., 2008). They solved the resulting inverse problem using a weighted damped least squares approach. Jiang et al. (2013) also performed an inversion utilizing a model made up of triangular dislocation elements, finding a solution using bounded variable least squares (Jiang et al., 2013). Fukahata and Wright (2008) aimed to improve the inversion of the slip distribution by treating the dip angle as a hyperparameter and estimating it using the Bayesian information criterion (Fukahata & Wright, 2008). This is followed by determining the slip distribution using maximum-likelihood methods. Their work is continued in another paper by Fukahata and Hashimoto (2016) who apply the same method to the 2016 Kumamoto earthquake (Fukahata & Hashimoto, 2016). Frietsch et al. (2019) extended the problem slightly, adding two new parameters for time-shift to the centroid time and the compensated-linear-vector-dipole (CLVD) component while also allowing for the parameters of multiple fault segments to be found at one time (Frietsch et al., 2019). This makes it possible for them to model a single event as multiple fault segments or model multiple separate events at the same time.

Finally, it should be noted that InSAR is not limited in usefulness to earthquake mechanism inversion, as shown by Peng et al. (2018) who used InSAR-derived deformation data to invert the mechanism of subsidence of Line 3 of the Xi'an metro near Yuhuazhai (Peng et al., 2018). They found from their inversion of a flat lying sill model with distributed contractions—with a depth based on the average depth of local pumping wells—that the rapid subsidence could be explained by excessive groundwater extraction in the area.

In this paper, a new approach that utilizes a genetic algorithm to simultaneously find the parameters of multiple point sources is introduced. As their name implies, genetic algorithms borrow their method of solving problems from genetics. A population of solutions to the problem is randomly generated, and they are allowed to crossover and mutate until an ideal solution is found. A crossover operator is the genetic algorithm equivalent of parents giving birth to offspring that inherit their genes. In a traditional genetic algorithm, a solution is represented as an array of bits, and the crossover operator might be defined to swap certain bits between two "parent" solutions. The mutation operator randomly changes the value of one or more bits in a solution array, similar to what occurs during a long period of a species's evolution. A genetic algorithm also requires some form of "survival of the fittest," which allows better solutions to be chosen to move forward during the execution of the algorithm. This is included in the algorithm as a cost function—more "fit" solutions to the problem are those who minimize the cost function or maximize some other desired measure of fitness (Kumar et al., 2010). In this paper, we utilize what is known as a real-coded genetic algorithm, in which the solutions are instead represented by a list of real-valued parameters. This change in the form of the solutions necessitates a change in the genetic operators, which will be explained in the next section.

2 Genetic Algorithm

As stated before, the solutions in a real-coded genetic algorithm are represented as lists of real-valued parameters. For the genetic algorithm used in this paper, the solutions are a list of parameters that describe the locations and orientations of a number of seismic point sources. In particular, every point source has a parameter for each of the following: x coordinate, y coordinate, z coordinate, strike angle, dip angle and seismic moment. The x, y and z coordinate parameters define the location of the point source in three-dimensional space where z = 0 defines the ground's surface in the case of zero deformation. The strike angle and dip angle determine the orientation of the slipping fault represented by the point source. Strike angle determines the direction of the line created by the intersection of the fault plane and the ground's surface. The dip angle is the angle between the fault plane and the ground's surface. In Okada's convention, the dip angle is restricted to lie within the range $0 < \delta < \frac{\pi}{2}$ (Okada, 1985). The seismic moment of a point source represents a combination of the fault area and the amount that it slips. A solution will have $6n$ parameters total, where n is the number of point sources the solution is composed of. These point sources give rise to surface deformation as defined by Okada's expressions for deformation due to shear and tensile faults in a half-space (Okada, 1985). The total deformation—the superposition of the deformation from all point sources—is compared to a desired surface deformation (the data), and the goal of the algorithm is to move and reorient the point sources until the model's surface deformation approximates that of the data. The specifics of the algorithm are discussed in the following paragraphs.

Given some ground deformation data in the form of ground coordinates and their corresponding deformations, the algorithm first determines the minimum and maximum x- and y-values to use as limits when generating possible source distributions to fit the data. This restricts the allowed locations of the point sources to an area below the ground deformation. Then the algorithm generates a population of a user-defined number of source distributions (models) containing a user-defined number of sources with random locations and orientations within specified limits. It calculates each model's displacement field, which is the ground deformation resulting from a superposition of the ground deformation due to individual point sources in the model. Each model is compared to the input data, and the chi-squared value of each model is recorded. In this paper, the chi-squared value for a given model is defined as:

$$\chi^2 = \sum_{i=1}^{n} (z_i - f(x_i, y_i))^2 \tag{1}$$

where z_i is the data value for the elevation of the ground at the point (x_i, y_i), $f(x_i, y_i)$ is the model value for the elevation of the ground at the point (x_i, y_i) and i runs over all data points.

After the chi-squared of each model has been determined, pairs of models are selected to use as parents in the creation of the next generation of models. The models with lower χ^2 are more likely to be selected as parents. Note that the same model cannot be both members of a pair, but can be present in more than one pair with another model. As each pair is selected, the member models are crossed to yield two more next-generation models.

This paper uses what is called a simulated binary crossover operator to generate new solutions based on the parent solutions (Deb & Agrawal, 1995). It is the real-coded equivalent of the single-point crossover operator of a binary genetic algorithm. The single-point crossover operator crosses the parent solutions by picking a random point in one solution's bit array, and swaps the bits after that point between the two solutions. Simulated binary crossover uses a probability density function to imitate single-point crossover for use in a real-coded genetic algorithm. Simulated binary crossover works as follows:

1. Choose two parents x_1 and x_2
2. Generate a random number $r \in [0, 1)$
3. Calculate the parameter β
$$\beta = \begin{cases} (2r)^{\frac{1}{\eta_c+1}} & \text{if } r \leq 0.5 \\ \left(\frac{1}{2(1-r)}\right)^{\frac{1}{\eta_c+1}} & \text{otherwise} \end{cases}$$
where η_c is the distribution index.
4. Compute the child solutions using
$$x_1^{new} = 0.5[(1+\beta)x_1 + (1-\beta)x_2]$$
$$x_2^{new} = 0.5[(1-\beta)x_1 + (1+\beta)x_2]$$

The distribution index determines the width of the distribution used for generating children. Large values of η_c tend to generate solutions closer to the parents, while smaller values generate solutions further away. The recommended value for η_c, and the one used in this paper, is $\eta_c = 2$ (Deb & Agrawal, 1995). Pairs are selected and crossed until the next generation becomes equal in size to the original population of models.

Once the next generation has been created, there is a user-defined chance for each model in the new generation to be mutated. The mutation operator, when applied to a model, gives each source in the model a user-defined chance to be shifted from its original position, orientation and seismic moment. The amount of translation or rotation is determined by a Gaussian random number generator centered at the original value of the coordinate. For example, if the original strike angle of a source is $\pi/2$, the Gaussian distribution used to select the new value has a mean value of $\pi/2$. The amount of shift in the location and seismic moment is selected in a similar manner. The process of crossing to create new generations and mutation of the new generations is repeated until the user-defined number of generations is reached.

3 Applying the Genetic Algorithm to Randomly Generated Data

To generate the synthetic data for testing the algorithm, an interferogram was generated by placing 10 point sources at random positions and orientations. The positions are restricted within a cuboid defined by the limits $0 < x < 30km$, $0 < y < 10km$ and $-10 < z < -3km$. The data points at which the generated data and models are compared lie within the same x and y bounds. 30 data samples were taken in the x-direction and 10 data samples in the y-direction, yielding a total of 300 data points—each a square with a side length of $1km$. The sources were placed with random strike and dip angles in the ranges $0 < \theta < 2\pi$ and $0 < \theta < \frac{\pi}{2}$, respectively, as well as random seismic moment in the range $10^8 < M_0 < 10^{12} Nm$. The total ground deformation was calculated as a result of the superposition of the ground deformation of all placed sources—with each point source causing a ground deformation according to Okada's equation for the vertical displacement of a strike-slip seismic source. Horizontal deformation was not considered in this example.

The generated interferogram was fit using 10 point sources. The starting values of the parameters in the initial population of solutions were chosen from uniform distributions for each parameter. As stated before, the x and y coordinates of the initial population of sources lie within the range of the data points. The initial depth of the sources and their initial strike and dip angles were restricted to the same ranges used to generate the interferogram. The algorithm ran for 10000 generations with the spreads in Table 1 used to mutate each parameter. In Table 1, the half order of magnitude spread for

Parameter	Amount of Spread
x	2 km
y	2 km
z	0.5 km
Strike angle	$\pi/6$
Dip angle	$\pi/24$
Seismic moment	Half order of magnitude

Table 1. The standard deviations of the Gaussian distributions used to mutate the parameters.

seismic moment means that the Gaussian was used to generate a power of 10 that was used as the new seismic moment. For example, if the original value of the seismic moment was 2.4×10^5, a Gaussian centered at $log_{10}(2.4 \times 10^5)$ with a standard deviation of 0.5 was used to generate a random number r. The new value of the seismic moment is then 10^r. The chance for a model to be chosen to mutate in a given generation was 20%. If chosen to mutate, each source point in the model had a 10% chance to have its location, strike angle, dip angle and seismic moment changed according to the above values of spread in each parameter. During the execution of the algorithm, the only restriction on the evolution of the sources is that their dip angles must remain in the range $0 < \delta < \frac{\pi}{2}$ as in Okada's convention—every other parameter is allowed to evolve freely according to the rules of the crossover and mutation operators. The model resulting from the fit is compared to the data in Figure 1.

4 Applying the Algorithm to ALOS-2 Data

The InSAR interferogram that was fit in this paper was processed by Lindsey et al. (2015a) and was downloaded from the Nepal Earthquake ALOS-2 InSAR website (Lindsey et al., 2015b). The particular one used was the sum of the ALOS2040533050-150222 and ALOS2050883050-150503 products, yielding an interferogram containing ground displacement between February 22nd, 2015 and May 17th, 2015. This interferogram was chosen because it exhibits deformation due to seismic events—in this case, the magnitude 7.8 earthquake that occurred on April 25th, 2015, 36 km east of Khudi, Nepal and its magnitude 7.3 aftershock that occurred on May 12th, 2015. The interferogram is a collection of points, each defined by their latitude, longitude and line-of-sight ground displacement. The line-of-sight displacement is converted to vertical displacement using the reported look angle of the satellite for each data point. To fit this interferogram, the data were binned into a 30-by-30 two-dimensional histogram to reduce the amount of computation time. The value of each bin was calculated as the average vertical displacement of each data point contained in that bin. After binning, the resulting pixels in latitude and longitude were mapped to the x-y plane, in units of km, to allow comparison to the results of the algorithm. When fitting this interferogram, the algorithm was set to use a population size of 500, with each solution in the population containing 15 seismic point sources. The earthquake was a result of thrust faulting (United States Geological Survey, 2015), and so Okada's equations for dip-slip faulting were used to calculate the ground deformation caused by the point sources. To further reduce computation time, the area of the interferogram being fit was reduced to pixels in the range $40 < x < 240km$ and $70 < y < 200km$, which contains the ground deformation of interest. For this example, only the vertical displacement of the ground was calculated—the horizontal displacement was not considered. After running for 15000 generations, taking about 7400s to run on a hexacore Intel i7-9750H CPU, the algorithm returned the model visible in Figure 2. This run of the algorithm used the same parameters for spread and mutation prob-

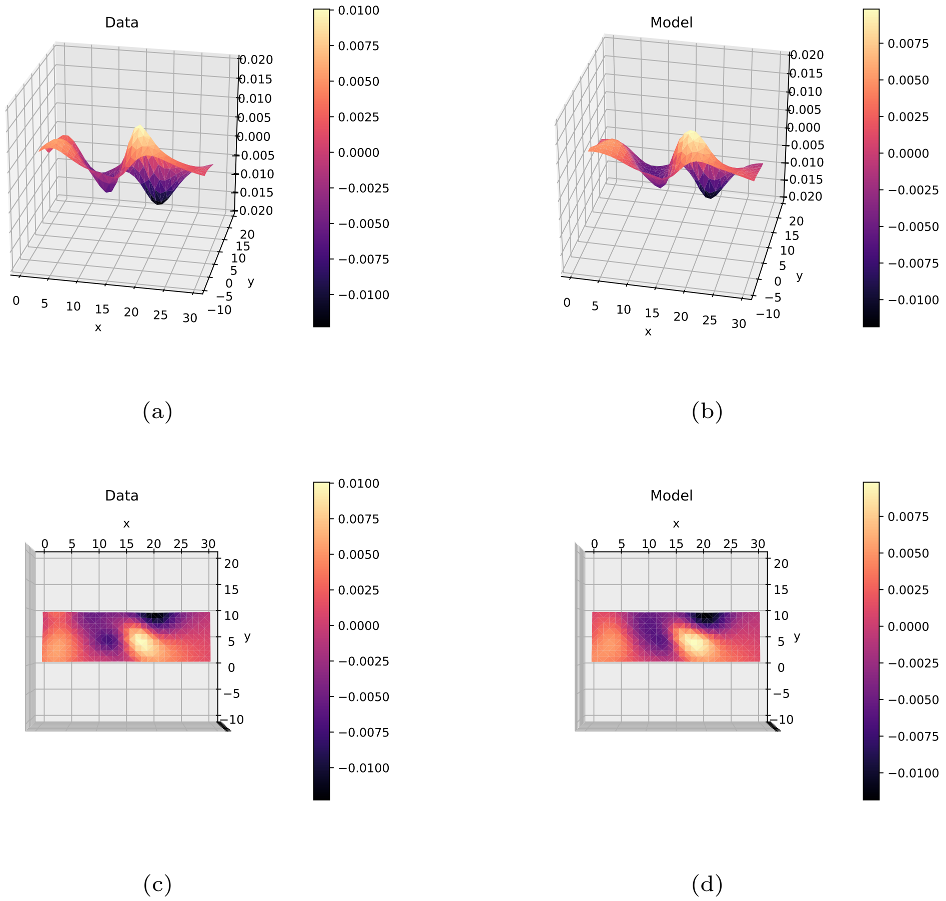

Figure 1. (a) Azimuthal view of the synthetic ground deformation data. (b) Azimuthal view of the model generated by the algorithm. (c) Top view of the synthetic ground deformation data. (d) Top view of the model generated by the algorithm.

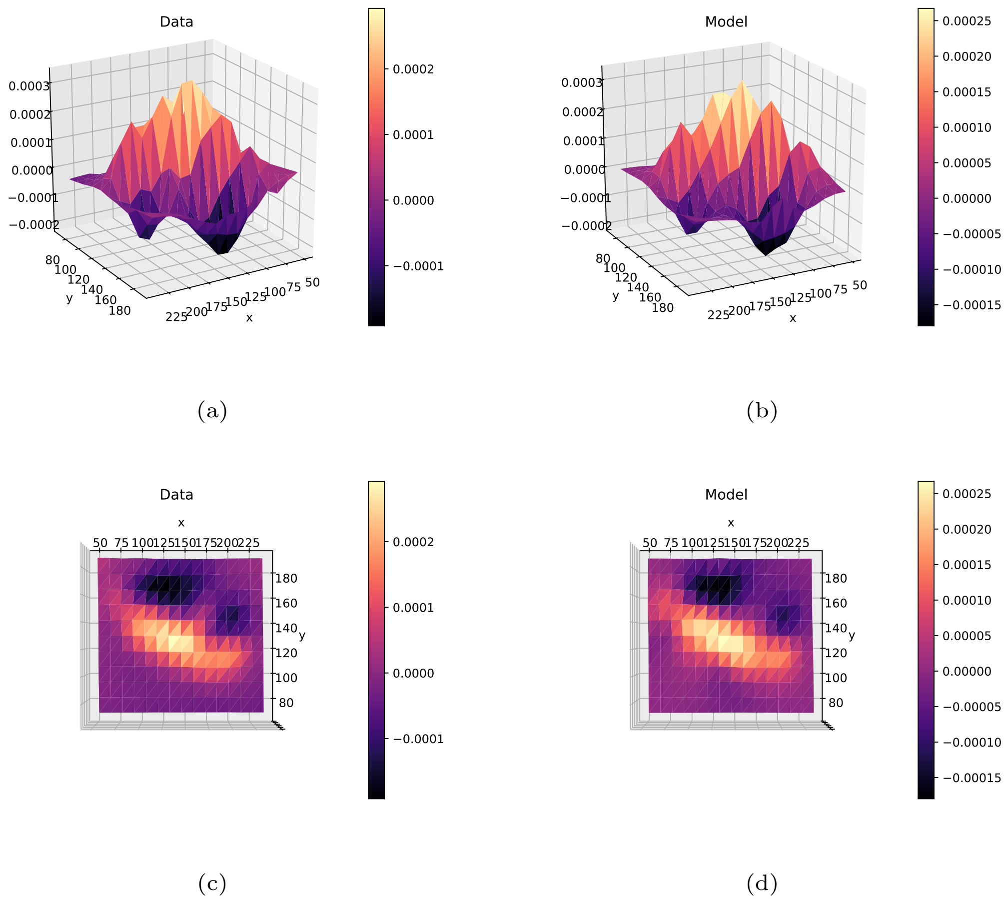

Figure 2. (a) Azimuthal view of the ALOS-2 ground deformation data. (b) Azimuthal view of the model generated by the algorithm. (c) Top view of the ALOS-2 ground deformation data. (d) Top view of the model generated by the algorithm.

ability as outlined in Table 1 and Section 3, respectively. The initial values of the point source parameters in the starting population were chosen from uniform distributions. The ranges of the x and y coordinates were limited to the dimensions of the interferogram area above and the depth ranged from $-30 < z < -20km$. The strike and dip angles ranged from $0 < \theta < 2\pi$ and $0 < \delta < \frac{\pi}{2}$, respectively. The seismic moments were pulled from the range $10^9 < M < 10^{12}Nm$. The parameters found by the algorithm for each point source can be seen in Table A1 in Appendix Appendix A.

5 Discussion and Conclusion

When comparing simulated or actual data to the resulting model, one can see that the basic shape of the data has been captured, but discrepancies exist if individual data points are compared. This is most likely a problem with the spread used when crossing and mutating the fit models. Since the spread of the parameters never changes, there comes a point where the error plateaus—further increases in fit accuracy require a decrease in the spread of the possible parameters. A larger initial spread is useful to widely search the parameter space for the appropriate fit and to prevent falling into a local minimum. However, a large spread also prevents the fit from settling to a more exact solution. Simply reducing the spread leads to an increase in the computation time, as more time will be required for the solutions to search the parameter space in smaller steps.

Increasing the population size can help widen the initial search area, but this also increases the computation time. A possible fix for this problem is an adaptive algorithm that modifies the spread during calculation to more efficiently search the parameter space and reduce the spread when close to the optimum solution. One such algorithm is outlined in (Deb et al., 2007).

The advantage of our method lies in its ability to invert InSAR data to obtain the parameters of more than one seismic source at a time. Inversions of fault geometry are typically calculated for a single rectangular fault plane, which limits their effectiveness in scenarios that are not well modeled by a single fault plane. One example is an interferogram that contains deformation from more than one significant seismic event, such as the one fit in Section 4, which contains deformation from both a magnitude 7.8 mainshock and a magnitude 7.3 aftershock. Another capability of point sources is modeling of faults that are not accurately portrayed by planar surfaces. The point sources move independently, so in theory they can model any possible fault shape if an appropriate number of sources are used. The cost of this increased flexibility is an increase in the amount of computation time required. The deformation caused by each source in a model must be calculated at every desired data point and their individual contributions must be summed to produce the total deformation field. This deformation field must be calculated for every model in the population for every generation that the algorithm runs. For example, if you desire for a population of 500 models containing 15 sources each to run for 10,000 generations, that is 75,000,000 function evaluations for each data point you are fitting. To reduce this computational complexity, it is possible to set a fixed value for any of the parameters or to use a more informative prior than a uniform distribution. This was not done in this paper to showcase the ability of the algorithm to fully explore the search space and arrive at a solution even with a vague starting point.

Acknowledgments

The data used in this paper was obtained from (Lindsey et al., 2015b). Cameron Saylor and John B. Rundle were supported by the National Aeronautics and Space Administration [grant number NNX17AI32G]. Portions of the research by Andrea Donnellan were carried out at the Jet Propulsion Laboratory, California Institute of Technology, under a contract with the National Aeronautics and Space Administration. None of the authors have identified financial conflicts of interest. We thank colleagues including Donald Turcotte for helpful discussions.

References

Bagnardi, M., & Hooper, A. (2018). Inversion of surface deformation data for rapid estimates of source parameters and uncertainties: A bayesian approach. *Geochem., Geophys., Geosyst.*, *19*(7), 2194-2211. doi: 10.1029/2018GC007585

Bürgmann, R., Rosen, P. A., & Fielding, E. J. (2000). Synthetic aperture radar interferometry to measure earth's surface topography and its deformation. *Ann. Rev. of Earth and Planet. Sci.*, *28*(1), 169-209. doi: 10.1146/annurev.earth.28.1.169

Deb, K., & Agrawal, R. (1995, 06). Simulated binary crossover for continuous search space. *Complex Sys.*, *9*(2), 115-148.

Deb, K., Sindhya, K., & Okabe, T. (2007). Self-adaptive simulated binary crossover for real-parameter optimization. In *Proc. of the 9th ann. conf. on genetic and evolutionary computation* (p. 1187–1194). doi: 10.1145/1276958.1277190

Feng, W., Li, Z., Elliott, J. R., Fukushima, Y., Hoey, T., Singleton, A., … Xu, Z. (2013). The 2011 M_w 6.8 Burma earthquake: fault constraints provided by multiple SAR techniques. *Geophys. J. Int.*, *195*(1), 650-660. doi: 10.1093/gji/ggt254

Frietsch, M., Ferreira, A. M. G., Funning, G. J., & Weston, J. (2019). Multiple fault modelling combining seismic and geodetic data: the importance of simultaneous sub-event inversions. *Geophys. J. Int.*, *218*, 958-976.

Fukahata, Y., & Hashimoto, M. (2016). Simultaneous estimation of the dip angles and slip distribution on the faults of the 2016 kumamoto earthquake through a weak nonlinear inversion of insar data. *Earth, Planets and Space*, *68*. doi: 10.1186/s40623-016-0580-4

Fukahata, Y., & Wright, T. J. (2008). A non-linear geodetic data inversion using abic for slip distribution on a fault with an unknown dip angle. *Geophys. J. Int.*, *173*, 353-364. doi: 10.1111/j.1365-246X.2007.03713.x

Hastings, W. K. (1970). Monte Carlo sampling methods using Markov chains and their applications. *Biometrika*, *57*(1), 97-109. doi: 10.1093/biomet/57.1.97

Jet Propulsion Laboratory, California Institute of Technology. (2014). *What is UAVSAR?* `https://uavsar.jpl.nasa.gov/education/what-is-uavsar.html`. ((accessed: 2020-06-16))

Jiang, G., Xu, C., Wen, Y., Liu, Y., Yin, Z., & Wang, J. (2013). Inversion for coseismic slip distribution of the 2010 M_w 6.9 Yushu Earthquake from InSAR data using angular dislocations. *Geophys. J. Int.*, *194*(2), 1011-1022. doi: 10.1093/gji/ggt141

Jo, M.-J., Jung, H.-S., & Yun, S.-H. (2017). Retrieving precise three-dimensional deformation on the 2014 m6.0 south napa earthquake by joint inversion of multi-sensor sar. *Sci. Rep.*, *7*. doi: 10.1038/s41598-017-06018-0

Kennedy, J., & Eberhart, R. (1995). Particle swarm optimization. In *Proc. of icnn'95 - int. conf. on neural networks* (Vol. 4, p. 1942-1948).

Kumar, M., Husain, M., Upreti, N., & Gupta, D. (2010). Genetic algorithm: Review and application. *J. of Inf. & Knowl. Management*.

Li, Z., Wen, Y., Zhang, P., Liu, Y., & Zhang, Y. (2020). Joint inversion of gps, leveling, and insar data for the 2013 lushan (china) earthquake and its seismic hazard implications. *Remote Sens.*, *12*(4), 715. doi: 10.3390/rs12040715

Lindsey, E. O., Natsuaki, R., Xu, X., Shimada, M., Hashimoto, M., Melgar, D., & Sandwell, D. T. (2015a). Line-of-sight displacement from alos-2 interferometry: M_w 7.8 gorkha earthquake and m_w 7.3 aftershock. *Geophys. Res. Lett.*, *42*(16), 6655-6661. doi: 10.1002/2015GL065385

Lindsey, E. O., Natsuaki, R., Xu, X., Shimada, M., Hashimoto, M., Melgar, D., & Sandwell, D. T. (2015b). *Nepal Earthquake ALOS-2 InSAR.* `https://topex.ucsd.edu/nepal/`. ((accessed: 2020-06-09))

Liu, X., & Xu, W. (2019). Logarithmic model joint inversion method for coseismic and postseismic slip: Application to the 2017 m_w 7.3 sarpol zahāb earthquake, iran. *J. of Geophys. Res.: Solid Earth*, *124*(11), 12034-12052. doi: 10.1029/2019JB017953

Okada, Y. (1985). Surface deformation due to shear and tensile faults in a half-space. *Bull. of the Seismol. Soc. of Am.*, *75*(4), 1135-1154.

Peng, M., Zhao, C., Zhang, Q., Zhang, J., & Liu, Y. (2018). Ground subsidence monitoring with mt-insar and mechanism inversion over xi'an, china. *ISPRS - Int. Archives of the Photogramm., Remote Sens. and Spatial Inf. Sci.*, *XLII-3*, 1375-1380. doi: 10.5194/isprs-archives-XLII-3-1375-2018

United States Geological Survey. (2015). *M 7.8 - 26km E of Khudi, Nepal.* `https://earthquake.usgs.gov/earthquakes/eventpage/us20002926/executive#general_summary`. ((accessed: 2020-06-10))

Wen, Y., Xu, C., Liu, Y., & Jiang, G. (2016). Deformation and source parameters of the 2015 m_w 6.5 earthquake in pishan, western china, from sentinel-1a and alos-2 data. *Remote Sens.*, *8*(2). doi: 10.3390/rs8020134

Zhang, L., Wu, J. C., Ge, L. L., Ding, X. L., & Chen, Y. L. (2008). Determining fault slip distribution of the chi-chi taiwan earthquake with gps and insar data using triangular dislocation elements. *J. of Geodyn.*, *45*(4-5), 163-168. doi: 10.1016/j.jog.2007.10.003

Appendix A Parameters found by the algorithm

	x	y	z	strike	dip	moment
1	69.8468	177.091	-29.9032	-0.45963	1.0839	0.13784
2	106.367	97.4588	-32.8588	6.61252	0.479722	168801
3	150.058	78.0384	-33.6847	19.0313	0.307234	1.23221e+09
4	140.425	191.588	-28.8003	5.79284	0.27404	1.90518e+10
5	202.588	127.159	-22.7864	0.111355	1.51411	2.05646e+10
6	72.8359	123.785	-17.2656	12.2768	1.4786	1894.74
7	131.227	132.126	-21.8409	6.72117	1.14697	1.06253e+10
8	143.966	118.57	-23.2668	3.75185	1.28514	1.53379e+10
9	73.7351	144.747	-21.1349	2.96139	1.4699	9.02219e+09
10	163.803	108.866	-29.3693	6.3945	0.352603	1.93104e+10
11	102.768	151.892	-22.8624	3.53234	0.0142592	2.29585e+10
12	181.87	89.2093	-36.7044	4.76648	0.0305045	4.18498e+09
13	126.37	151.843	-27.464	0.494327	1.51399	2.4217e+10
14	237.313	230.565	-26.7075	0.469047	1.12608	5.72458e+09
15	143.542	133.469	-26.0931	6.43808	1.21437	626.352

Table A1. The parameters found by the algorithm for each point source in the ALOS-2 data fit. The strike and dip angles are recorded in radians and seismic moment in Nm. Recall that these parameters use Okada's convention, where a strike angle of zero means the strike is parallel to the x axis.

Appendix B Residuals between data and models

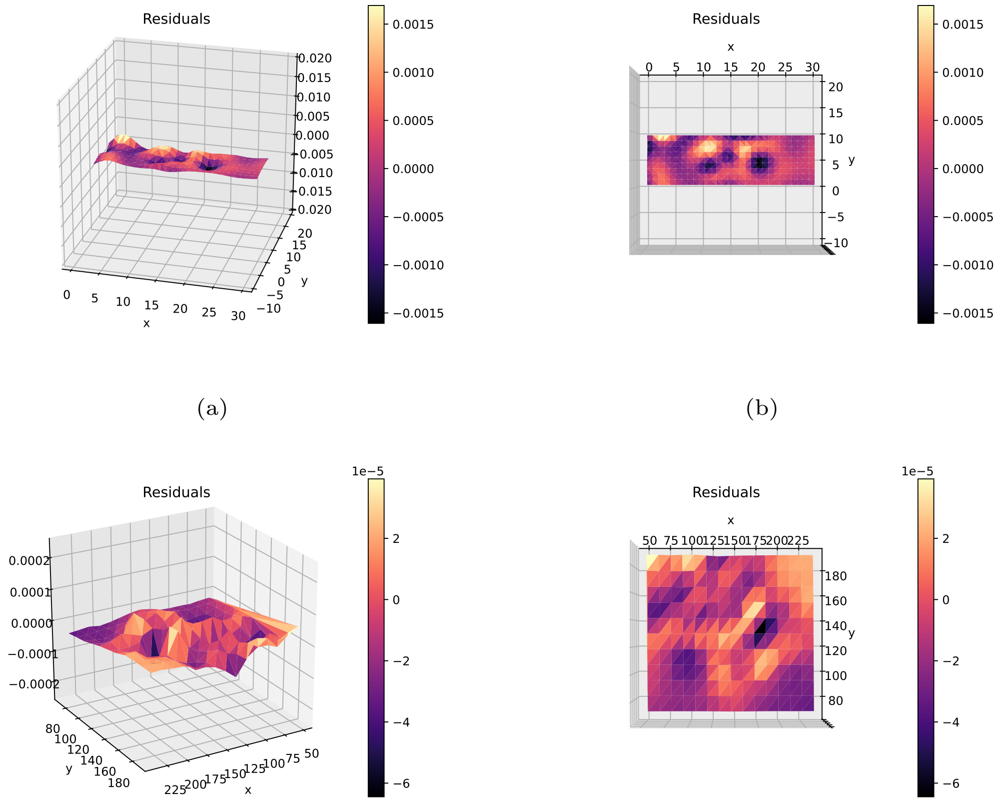

(a) (b) (c) (d)

Figure B1. (a) Azimuthal view of the residuals between the synthetic ground deformation data and the corresponding model. (b) Top view of the residuals between the synthetic ground deformation data and the corresponding model. (c) Azimuthal view of the residuals between the ALOS-2 ground deformation data and the corresponding model. (d) Top view of the residuals between the ALOS-2 ground deformation data and the corresponding model.